bioRxiv preprint doi: https://doi.org/10.1101/2022.11.14.516510; this version posted November 14, 2022. The copyright holder for this preprint (which was not certified by peer review) is the author/funder, who has granted bioRxiv a license to display the preprint in perpetuity. It is made available under aCC-BY-NC-ND 4.0 International license.

TITLE: Circuit-specific selective vulnerability in the DMN persists in the face of widespread amyloid burden.

AUTHOR NAMES AND AFFILIATIONS: Samuel J. Brunwasser[1], Clayton Farris[1], Halla Elmore[1], Eva L. Dyer[2], Kiran Bhaskaran Nair[1], Jennifer D. Whitesell[3,4], Julie A. Harris[3,4], Keith B. Hengen[1]*

[1]Department of Biology, Washington University in Saint Louis, Saint Louis, MO

[2]Department of Biomedical Engineering, School of Electrical & Computer Engineering; Georgia Institute of Technology; Atlanta, GA, 30332; USA

[3]Allen Institute for Brain Science, Seattle, WA

[4]Cajal Neuroscience, Seattle, WA

*Corresponding Author

ABSTRACT

The relationship between brainwide functional decline and accumulation of pathological protein aggregates in Alzheimer's disease (AD) is complex and not well understood. A set of highly interconnected cortical regions known as the default mode network (DMN) exhibits selective vulnerability to both functional decline and amyloid beta (Aβ) plaques in early AD. One possibility is that early Aβ accumulation in the DMN drives vulnerability. However, it is unknown whether there is something intrinsic to neuronal projections within the DMN that biases these circuits towards dysfunction. Here we directly test this hypothesis using long-term recordings of the spiking activity of ensembles of single units in freely behaving mice characterized by global cortical and hippocampal Aβ burden (APP/PS1). Specifically, we track the interactions of a population of neurons within a DMN region and two additional populations that comprise monosynaptic targets, one within and the other outside the DMN. In addition, we record single neurons in hippocampus and examine interactions between in-DMN and out-DMN cortical circuits triggered on hippocampal sharp-wave ripples, stereotyped hippocampal events that contribute to memory consolidation in the cortex. We examine the statistics of local activity as well as inter-regional communication in a region, genotype, and brain-state dependent manner. Our data reveal dysfunction restricted to in-DMN projecting circuits. In contrast, communication along neuronal projections that originate in the DMN but target out-DMN populations are equivalent in APP/PS1 and WT mice. Circuit dysfunction is most evident throughout sleep as well as within sharp-wave ripples. Our results indicate that cells in the DMN exhibit differential intrinsic vulnerability to amyloid injury dependent on their projection targets.

KEYWORDS: Default mode network, amyloid beta, sleep, systems, selective vulnerability, single neuron

bioRxiv preprint doi: https://doi.org/10.1101/2022.11.14.516510; this version posted November 14, 2022. The copyright holder for this preprint (which was not certified by peer review) is the author/funder, who has granted bioRxiv a license to display the preprint in perpetuity. It is made available under aCC-BY-NC-ND 4.0 International license.

INTRODUCTION

The default mode network (DMN) is a set of distributed but highly interconnected brain regions that are coactivated during wakeful rest (Raichle et al., 2001). In addition to its role in cognition, the DMN is noteworthy as it is selectively vulnerable to the early stages of neurodegenerative disease. Specifically, in Alzheimer's Disease (AD), amyloid-beta (Aβ) accumulation starts in DMN hubs and propagates to secondary regions along anatomical connections (Braak et al., 2013; Jucker and Walker, 2013; Walker and Jucker, 2015). Unsurprisingly, brain regions that accumulate Aβ show disrupted activity (Sheline et al., 2010); disrupted functional connectivity between DMN regions is a hallmark of early AD (Agosta et al., 2012).

The simplest explanation is that changes in the DMN are purely and directly a result of Aβ. This rationale supports the prediction that Aβ deposits in other circuits would render them similarly disrupted. Alternatively, early AD represents the confluence of two events. Specific circuits are intrinsically vulnerable to Aβ-related damage, and it is in these circuits that Aβ takes hold. In this case, if Aβ deposits were widespread, DMN circuitry would still be disrupted relative to non DMN regions. However, because Aβ deposition is restricted to the DMN early in AD, it is difficult to separate the local impact of Aβ from an intrinsic vulnerability of these brain regions. Either possibility has powerful implications for an understanding of AD etiology and intervention strategies. Here we take advantage of a model of widespread amyloidosis and long-term, multi-site recordings spanning in-DMN and out-DMN circuits to directly test the hypothesis that neurons in the DMN are intrinsically vulnerable independent of Aβ.

The regions comprising the DMN exhibit a high degree of reciprocal connectivity (Horn et al., 2014; Hagmann et al., 2008; Greicius et al., 2009), such that the majority of DMN efferents target other DMN regions. Nonetheless, a minority of DMN projection neurons target postsynaptic sites broadly throughout the brain (Whitesell et al., 2021). In both cases, the cell bodies lie within the anatomical borders of the DMN, but the circuits are divisible by postsynaptic target; in-DMN projections originate and terminate in DMN regions, while out-DMN projections terminate in non-DMN regions. If DMN neurons are intrinsically vulnerable to Aβ-related dysregulation, the dissociation of DMN and non-DMN circuitry by projection target raises an interesting possibility: the cellular impact of disease may be conditioned on axonal target, even when comparing adjacent neurons.

The recent discovery of two neuronal populations in the mouse ventral retrosplenial cortex (RSPv), a core DMN region, reveals such intermingled circuitry (Whitesell et al., 2021). Both subpopulations are composed of excitatory projection neurons, but differ in their postsynaptic targets. One group, the in-DMN targeting, sends monosynaptic connections to dorsal anterior cingulate (ACAd), another selectively vulnerable DMN region. The other group, the out-DMN targeting, sends monosynaptic connections to primary visual cortex (VISp), which is outside of the DMN. This anatomy crystalizes the question of selective vulnerability, allowing for interrogation not only of region but also of connectivity.

For three reasons, this circuitry, in combination with the APP/PS1 mouse, is ideally suited to test whether neurons in the DMN are intrinsically vulnerable during disease or if vulnerability is caused by the anatomical pattern of Aβ deposition. First, the APP/PS1 mouse overexpresses amyloid precursor protein (APP) and is remarkable for indiscriminate Aβ accumulation throughout the cortex and hippocampus (Whitesell et al., 2019). This deposition pattern thus circumvents the confounding restriction of Aβ to the DMN. Second, mouse models are amenable to multi-site recording of ensembles of single neurons, allowing for the simultaneous monitoring of multiple monosynaptically connected populations in the context of freely behaving animals. Finally, the APP/PS1 mouse is a model of early AD progression, such that disruptions in cortical physiology are not explained by neuron loss (Rupp et al., 2011).

Here we collected and analyzed four-site recordings of neuronal ensembles in APP/PS1 mice to test the hypothesis that in- and out-DMN circuits are differentially vulnerable in the context of a global amyloid burden. We conducted long-term, simultaneous recordings of extracellular spiking from ensembles of single neurons in RSPv, ACAd, VISp, and hippocampus (CA1) of freely behaving adult WT and APP/PS1 mice. We examine neuronal dynamics and circuit interactions as a function of brain state over a 24 h cycle containing a full range of naturally occurring behaviors. Our results reveal that, in contrast to adjacent out-DMN projecting

bioRxiv preprint doi: https://doi.org/10.1101/2022.11.14.516510; this version posted November 14, 2022. The copyright holder for this preprint (which was not certified by peer review) is the author/funder, who has granted bioRxiv a license to display the preprint in perpetuity. It is made available under aCC-BY-NC-ND 4.0 International license.

neurons, in-DMN projections are selectively disrupted in a sleep-dependent manner. These data indicate intrinsic vulnerability to amyloidosis that is determined by projection target.

RESULTS

Chronic Monitoring of Single Neuron Activity in Four Brain Regions in WT and APP/PS1 Mice

Mice harboring the APP/PS1 transgenes exhibit increased brain Aβ by 8 months and neuritic plaques in the isocortex by 10 months of age (Trinchese et al., 2004). While Aβ expression is constrained to the DMN in the earliest stages of human AD, we observed plaques throughout the APP/PS1 isocortex and hippocampus (Figure S1A-B) as described previously (Whitesell et al., 2019). To test the hypothesis that circuits whose source and target are within the DMN are intrinsically vulnerable to amyloidosis injury, we performed continuous (10-20 d), multisite recordings of extracellular signals from ACAd, RSPv, VISp, and CA1 (Figure 1A-B) in APP/PS1 and WT littermates between the ages of 12-16 months (n = 4 WT, n = 4 APP/PS1).

Single units were extracted with MountainSort-based clustering (Chung et al., 2017) and labeled automatically by a random forest trained on measures of cluster quality and isolation such as L-ratio, Mahalanobis distance, and the absolute refractory period (Figure 1C,D). Regular spiking units (RSUs, ~90% pyramidal) were classified based on waveform (Hengen et al., 2013; Cardin et al., 2007; Niell and Stryker, 2008). In addition, high frame-rate video was collected and processed with a convolutional neural network to track animal movements ranging from respiratory-related to locomotion (Mathis et al., 2018). This was combined with electrophysiological signals low-passed at 60 Hz for sleep scoring as described previously (Figure S1F-G; Hengen et al., 2016). Here we analyze 24 h of data from each animal, collected at least 1 w into the recording. Analyses are restricted to well-isolated RSUs with a presence ratio of at least 90% (i.e., included neurons exhibited detectable activity for the entire period of analysis). Each animal's RSPv ensembles contained single units with short-latency interactions (significant single neuron pairwise correlations at <10 msec) within both ACAd and VISp, consistent with monosynaptic excitatory connectivity. These results are a functional confirmation of independent populations linked by monosynaptic projections as described previously (Whitesell et al., 2021).

Hyperexcitability is restricted to DMN circuitry in APP/PS1 mice

Prior works examining basic measures of neuronal activity in mouse models of APP overexpression have yielded conflicting results. Measurement of calcium transients across frontal cortex and CA1 suggest hyperexcitability (Busche et al., 2008; 2012), while extracellular recordings in frontal cortex indicate hypoexcitability (Klee et al., 2020). Experimental constraints, such as head-fixation and relatively short recordings, make it difficult to reconcile these findings. One possibility is that there are circuit-specific and context-dependent differences in the impact of amyloidosis on neuronal activity. To understand whether APP overexpression impacts neuronal firing rates in the intact brain of freely behaving animals over ethologically relevant time scales, we examined single neuron activity as a function of brain region, arousal state, and genotype.

Across sleep and wake, we observed no significant effect of genotype on the mean firing rates of neurons in VISp, a non-DMN region. In contrast, the DMN hub regions of ACAd and RSPv exhibited increased single unit activity, but only during waking (Figure 1F. Wilcoxon rank sum with Bonferroni correction ACAd: Wake p=3.18e-5, NREM p=0.079, REM p=0.03; RSPv: Wake p=0.002, NREM p=0.096, REM p=0.165; VISp: Wake p=0.079, NREM p=0.222, REM=0.057). These results are unlikely to arise from gross Aβ-related damage; single neuron yield did not differ by genotype (Figure S1D), consistent with a lack of cell loss at 1y.

bioRxiv preprint doi: https://doi.org/10.1101/2022.11.14.516510; this version posted November 14, 2022. The copyright holder for this preprint (which was not certified by peer review) is the author/funder, who has granted bioRxiv a license to display the preprint in perpetuity. It is made available under aCC-BY-NC-ND 4.0 International license.

Neuron counts in representative histology were similar in each recorded region (Figure S1C). Taken together, these results suggest that neurons within DMN brain regions may be selectively sensitive to Aβ burden.

Timing within in-DMN but not out-DMN circuitry is disrupted in APP/PS1 mice

While ensemble mean firing rates were elevated in DMN regions, these results cannot distinguish neurons that participate in distinct circuits. To directly address the question of whether vulnerability within the DMN depends on connectivity, we performed lagged pairwise spike correlation between all pairs of single units in monosynaptic in-DMN circuitry (RSPv to ACAd) and out-DMN circuitry (RSPv to VISp). Crucially, the source of each of these circuits is the same (RSPv) such that the local environment of the recorded neurons did not differ by circuit. We measured the magnitude and directionality (delay) of the source/target interaction as a function of genotype and arousal state (420 wake epochs, 832 NREM epochs) (Figure 2A).

Consistent with prior reports of broadly increased functional connectivity (Shah et al., 2018), relative to WT mice, in-DMN and out-DMN circuits in APP/PS1 animals exhibited an increased correlation magnitude in both wake and NREM (Figure 2B, S5; Wilcoxon rank sum with Bonferroni correction RSP-ACAd Wake $p = 0.018$, NREM $p = 0$, RSP-VISp Wake $p = 3e\text{-}6$, NREM $p = 0$). Within this context, we examined the temporal dynamics of inter-regional communication. In the out-DMN circuit, there was no difference between WT and APP/PS1 in the timing of the source/target interaction. This suggests that, while potentially carrying a stronger signal in APP/PS1 animals, the cellular mechanisms supporting communication in out-DMN circuits are equivalent to WT animals.

In contrast, the timing of in-DMN circuit communication was significantly altered in APP/PS1 animals relative to WT. Specifically, the APP/PS1 in-DMN circuit was characterized by a lag (3 ms in wake, 5 ms in NREM) suggestive of increased feedforward drive from RSPv to ACAd (Figure 2B,C; peak offset Wilcoxon rank sum with Bonferroni correction RSP-ACAd Wake $p = 6.61e\text{-}8$, NREM $p=0$). These data reveal an in-DMN circuit-specific lagging in a posterior to anterior direction, with greatest severity during NREM sleep. These results suggest that selective vulnerability is not explained by differential Aβ exposure or coarse anatomical location, but is a property of connectivity.

Epochs of wake and NREM encompass diverse contexts and substates and can last for thousands of seconds. These results suggest that communication structure broadly is disrupted in in-DMN circuitry of APP/PS1 mice, but offer little insight into the disruption of specific neurophysiological processes.

The timing of sharp-wave ripple-driven spiking in RSPv is aberrant in APP/PS1 animalsHippocampal sharp wave ripples (SWRs) are large oscillations (140-220 Hz) that arise from the dendritic layer of CA1. SWRs are observed primarily during NREM sleep, and are involved in memory consolidation between the hippocampus and cortex (Girardeau et al., 2009). The discrete, aperiodically repeating nature of SWRs presents an opportunity for precise trial-structure with cognitive relevance in long term recordings of freely behaving animals. To understand intra-regional communication in this context, we first identified ripples in broadband CA1 data during NREM epochs using standard algorithms (Figure 3A,B; Karlsson et al., 2009). We observed no significant effect of genotype on SWR frequency, amplitude, and duration, although there was noteworthy inter-animal variability in all three measures, particularly in WT animals (Zhurakovskaya et al., 2019, but see Cushing et al., 2020) (Figure S3A-C, Wilcoxon rank sums ripple density $p = 0.441$, ripple duration $p = 0.054$, ripple amplitude $p = 0.923$).

While SWRs are generated in the hippocampus, one of the major inputs to RSP is a monosynaptic projection from CA1 (Yamawaki et al., 2019), and SWR driven spiking in RSP has been described previously

bioRxiv preprint doi: https://doi.org/10.1101/2022.11.14.516510; this version posted November 14, 2022. The copyright holder for this preprint (which was not certified by peer review) is the author/funder, who has granted bioRxiv a license to display the preprint in perpetuity. It is made available under aCC-BY-NC-ND 4.0 International license.

(Opalka et al., 2020). In our data, individual neurons in RSP displayed increased firing around the time window of hippocampal SWRs (Figure 3C,E).

We reasoned that, in the context of general sleep and wake, in-DMN circuitry was delineated from out-DMN circuitry by perturbation of the timing of intraregional communication. The hippocampus is sometimes considered part of the DMN (Alves et al., 2019), thus we hypothesized that the timing of SWR activation of RSPv and ACAd but not VISp should be aberrant in APP/PS1 animals relative to WT. In line with our hypothesis, the timing of SWR-related activity in VISp did not differ by genotype (Figure 3D; Median peak time WT 2 +/- 4.9 ms, APP 2 +/- 3.3 ms, p =0.348 Wilcoxon rank sum). However, in APP/PS1 animals, the SWR peak in RSPv was accelerated (Figure 3E; median peak time WT 13 +/- 3.2 ms, median peak time APP -8 +/- 2.2 ms, p = 3.29e-8 Wilcoxon rank sum). In addition, SWR-related spiking in RSPv of APP/PS1 animals was also characterized by a second, slower peak that was not observed in WT animals. Further, we observed a large delay in the timing of SWR-associated spiking in ACAd (Figure 3F; median peak time WT -74 +/- 4.9 ms, APP 5 +/- 3.3 ms, p = 6.73e-11 Wilcoxon rank sum).

Consistent with our observations of a global increase in pairwise correlations, the response of RSP neurons in APP/PS1 animals to SWRs was exaggerated relative to WT (Figure 3E; peak height Wilcoxon rank sum p = 1.24e-8; median peak height WT = 4.52, APP = 6.50). This effect was similar in ACAd and VISp but to a lesser extent (Figure 3D-F). Taken together, these results suggest that Aβ enhances SWR driven spiking in RSPv, and that the CA1 to RSPv and ACAd circuits show in-DMN-like disruptions in the timing of communication.

Reduced communication dimensionality in in-DMN circuits relative to out-DMN circuits in APP/PS1 animals

While these data suggest that hippocampal projections to DMN regions are intrinsically vulnerable to Aβ, it is unclear whether altered timing implies a disruption in the information content carried along a circuit. To understand how Aβ impacts inter-regional communication as a function of in- versus out-DMN circuitry, we took advantage of the trial-like structure provided by SWR-driven activity in all recorded regions to measure the dimensionality of the communication subspace between each pair of regions. To do this, performed reduced rank regression between source and target regions of the in-DMN and out-DMN circuits (Semedo et al., 2019). Regression performance or the degree to which source activity predicted target activity, was measured as a function of the rank of the coefficient matrix (i.e., the number of predictive dimensions). The number of source dimensions at which regression performance drops below that of the full rank model indicates the number of predictive dimensions needed to fully capture the interaction of the two regions (Figure 4A,B). In simple terms, complex patterns of activity require more dimensions to reproduce than simple patterns.

Despite the fact that SWR-driven spiking was increased in all recorded regions in APP/PS1 mice relative to WT (Figure S3D-F), the dimensionality of RSPv to VISp interaction (out-DMN) was equivalent across genotype (Figure 4A; p=0.122 Wilcoxon rank sum). However, the dimensionality of RSPv to ACAd interaction (in-DMN) was significantly reduced in APP/PS1 animals (Figure 4B; p = 6.16e-5 Wilcoxon rank sum). These data indicate that the complexity of communication during memory-related neurophysiological events is diminished by Aβ specifically in in-DMN circuitry. It is equally noteworthy that, in the 12-15 mo APP/PS1 mouse, widespread Aβ does not impact out-DMN communication.

DISCUSSION

The brain regions comprising the default mode network (DMN) are selectively vulnerable to Aβ deposition and AD-related disruption. This vulnerability has been widely described, particularly in human clinical populations, yet it has been challenging to separate two possible explanations of this phenomenon. The simplest case is

bioRxiv preprint doi: https://doi.org/10.1101/2022.11.14.516510; this version posted November 14, 2022. The copyright holder for this preprint (which was not certified by peer review) is the author/funder, who has granted bioRxiv a license to display the preprint in perpetuity. It is made available under aCC-BY-NC-ND 4.0 International license.

that the pattern of Aβ deposition early in Alzheimer's Disease (AD) determines the pattern of affected circuits. In other words, Aβ plaques are toxic to nearby neurons, and plaque expression is limited to the DMN. Alternatively, early AD represents the confluence of two events. Specific circuits are intrinsically vulnerable to Aβ-related damage, and it is in these circuits that Aβ takes hold. To directly test which of these explanations is more likely, we made four-site recordings of neuronal ensembles in individual APP/PS1 mice, which are characterized by a widespread Aβ burden across the isocortex and hippocampus. Our data reveal surprising differences in neural activity that are modulated by whether neurons are projecting to in-DMN or out-DMN targets. Not only do our data offer a unique resolution of intraregional circuitry in an animal model of AD, but our recordings span 24 h of unrestrained, natural behavior. In this context, DMN circuit-specific disruptions appear to be exaggerated throughout NREM sleep, and are evident when examined in the context of sharp-wave ripples (SWRs), a neurophysiological event with consequences for memory consolidation. Because our electrodes did not cover all DMN regions, more work will be required to understand if our data generalize.

Many mouse models of AD rely on the transgenic overexpression or knock-in of humanized APP carrying familial disease mutations that increase Aβ production. Lines differ in the anatomical distribution and timing of plaque deposition (Whitesell et al., 2019; Xia et al. 2021), as well as the timing and extent of behavioral, functional, and cellular damage. The APP/PS1 mouse used in this study accumulates plaque in the cortex and hippocampus first with widespread coverage, yet minimal degenerative damage, at 12-16 months of age (Rupp et al., 2011). Similarly, we detected no significant differences in the yield of single units or histology as a function of genotype that might have indicated neuronal loss. The broad anatomical expression of APP/Aβ in these mice is related to the prion promoter used to drive the transgenes; an important caveat that is often considered undesirable for modeling natural human disease progression. Here we leverage this feature in a positive light to address an important question about circuit vulnerability to Aβ injury.

While APP overexpressing mice exhibit relatively little neurodegeneration, there is evidence of neuronal dysfunction by 12 months in the APP/PS1 line. These animals experience frequent spontaneous epileptiform discharges on EEG as well as seizures, which we noted in our observations of behavior and physiology (Minkeviciene et al., 2009). In the APP/PS1 mouse, Aβ has been shown to increase neuronal activity (Busche et al., 2008; 2012) as well as decrease neuron firing, perhaps explained by a neuron's proximity to nearby plaques (Klee et al., 2020). This may also depend on brain state or context (Zarhin et al., 2022), highlighting the need to examine neuronal activity in multiple regions across a range of naturally occurring conditions. At a lower spatial resolution, APP overexpression reduces the power of gamma oscillations (Palop and Mucke, 2016) and alters coupling between the hippocampus and cortex during sleep (Zhurakovskaya et al., 2019). Our results suggest that alterations in activity are likely to be circuit-specific and may require simultaneous monitoring of multiple populations of neurons.

The major impact of pathology, especially early in disease progression, may vary throughout the circadian cycle and related changes in brain state and behavior. Our data emphasize a key role for brain state in understanding amyloidosis. Specifically, our results reveal that in-DMN dysfunction is pronounced during NREM sleep. This is of particular interest in light of the relationship of NREM sleep to memory. Much work has linked sleep, particularly NREM, to memory consolidation (Rasch and Born, 2013) often involving hippocampal-cortical interactions (McClelland and O'Reilly, 1995). Perhaps it is unsurprising then that early AD in humans is marked by disrupted sleep structure (Ju et al., 2013; Warren et al., 2013; Lim et al., 2014). This is likely a bidirectional interaction, as chronically disrupted sleep is predictive of disease (Bokenberger et al., 2018). Similarly, APP/PS1 mice show disrupted sleep/wake cycles (Roh et al., 2012).

bioRxiv preprint doi: https://doi.org/10.1101/2022.11.14.516510; this version posted November 14, 2022. The copyright holder for this preprint (which was not certified by peer review) is the author/funder, who has granted bioRxiv a license to display the preprint in perpetuity. It is made available under aCC-BY-NC-ND 4.0 International license.

Even within sleep, pathology may be best understood in the context of discrete events. Our data suggest that, in APP/PS1 animals, the timing of SWR driven activity is disrupted in cortical regions that comprise the DMN but is intact in non-DMN cortices. Further, the dimensionality of communication in in-DMN circuits is significantly reduced while out-DMN circuits are equivalent to WT. The suggestion that SWRs are a locus of pathological effect is consistent with observations of abnormal SWR properties in mouse models of a range of neurodegenerative diseases (Zhurakovskaya et al., 2019; Witton et al., 2016; Jura et al., 2019). In the APP/PS1 RSPv, our results reveal an interesting detail: neuronal firing is elevated during SWRs but not during general NREM sleep. This suggests that RSPv is not tonically hyperactive but has exaggerated responses when activated, consistent with impaired feedforward inhibitory input from CA1 (Yamawaki e t al., 2019; Opalka et al., 2020). Further work is required to test the hypothesis that disruption in the balance of excitation and inhibition (Palop and Mucke, 2016) may be restricted to brain states or events (Kaefer et al., 2022).

Our findings are reminiscent of the cascading network failure hypothesis in AD (Jones et al., 2016). This asserts that AD pathogenesis is the result of network failures, beginning in the posterior DMN, that shift processing burden to the next step of the system, which subsequently fails as the damage propagates along lines of high connectivity (i.e. through the DMN, initially). This model predicts increases in connectivity that precede structural and functional disruption, and accounts for the prion-like spread of Aβ (Braak and Braak, 1991; Warren et al., 2013). Key to this theory is that altered functional communication between DMN regions is an inciting event. Consistent with this, our data confirm increased functional connectivity and impaired communication in the in-DMN pathway, despite equivalent amyloid burden in the off-DMN pathway. Also of note, our data reveal lagged connectivity in the direction of RSPv to ACAd (posterior to anterior DMN), which is also consistent with data from humans with AD (Jones et al., 2016). The consistency of our observations and key features of human pathology suggests that the mechanisms underlying the selective vulnerability of DMN circuits are phylogenetically conserved and are not tethered to the specifics of the disease process.

We propose that in AD, the selective vulnerability of the DMN is a consequence of intrinsic vulnerability to injury and is not explained by the anatomical specificity of amyloid accumulation. Within DMN regions, the vulnerability of individual neurons to functional disruption is like to be determined by the gene expression underlying connectivity patterns (Whitesell et al., 2021; Chen et al., 2022). The advent of new technologies in measuring mesoscale connectivity, recording neuronal activity, and resolving spatial transcriptomics will make it possible to further disentangle to cellular and circuit rules disease spread through the DMN.

bioRxiv preprint doi: https://doi.org/10.1101/2022.11.14.516510; this version posted November 14, 2022. The copyright holder for this preprint (which was not certified by peer review) is the author/funder, who has granted bioRxiv a license to display the preprint in perpetuity. It is made available under aCC-BY-NC-ND 4.0 International license.

FIGURE 1

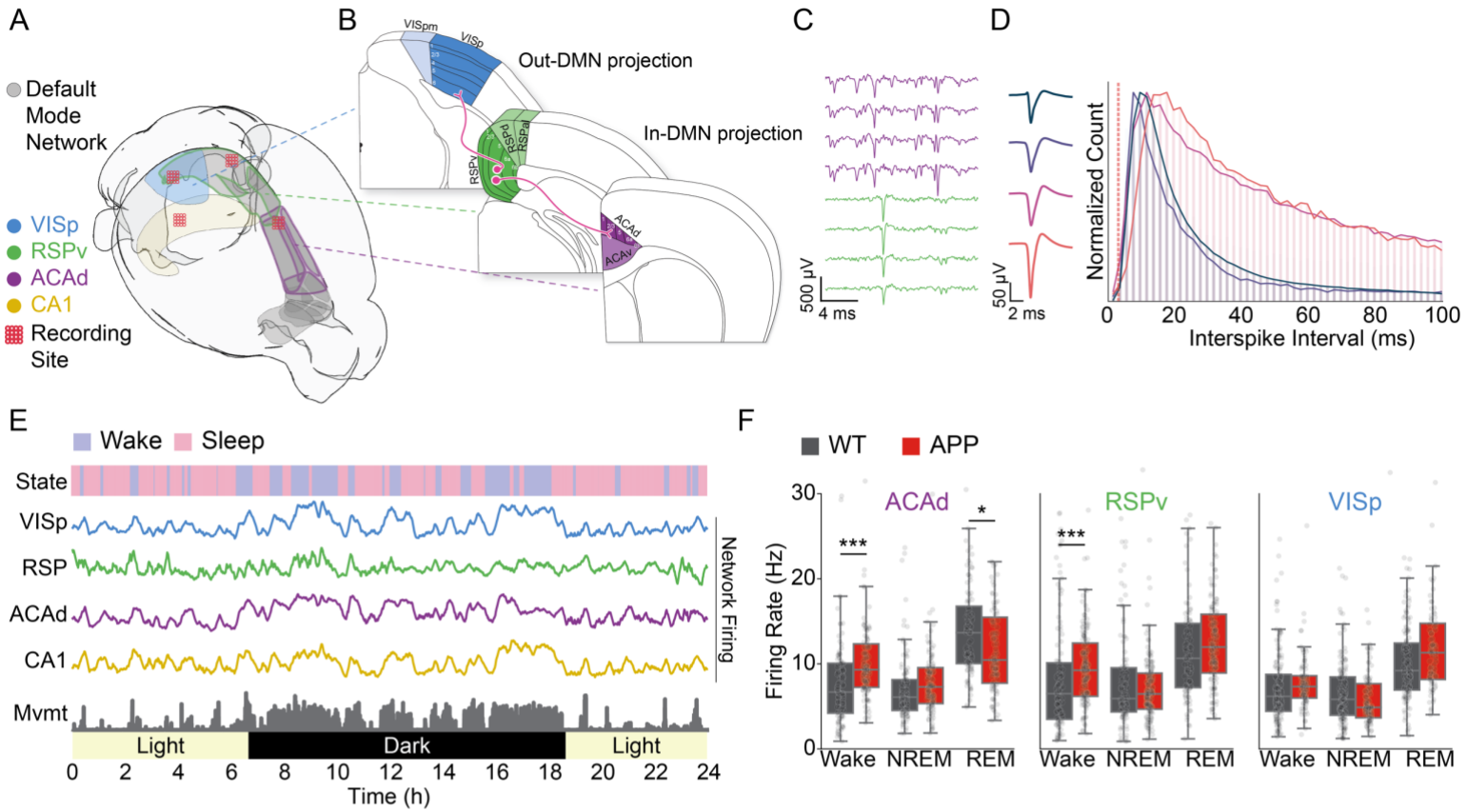

Figure 1: Aβ overexpression drives increased neuronal activity in DMN regions as a function of brain state. A) Experimental overview. 64 ch tetrode bundles were implanted in four brain regions (total of 256 ch), two in the default mode network (DMN; RSPv, ACAd), one outside of the DMN (VISp), as well as CA1 hippocampus. B) Illustration of the monosynaptic projection connecting populations in RSPv to ACAd (in-DMN) and population in RSPv to VISp (out-DMN). C) Example raw data trace from two tetrodes, one in RSPv and the other in ACAd. D) (left) four mean waveforms of single units recorded on one tetrode and their (right) interspike interval histograms which reveal a refractory period. Vertical dashed red line indicates minimum possible refractory period for a single unit. Colors in the histogram correspond to the 4 unit waveforms on the left. E) 24 h of data from a single animal. Rows denote sleep/wake states, mean ensemble firing rate by region, animal locomotion ("movement"), and environmental conditions (light/dark). F) Mean firing rate of all single units as a function of genotype, region, and brain state (* $p < 0.05$,*** $p < 0.001$; Wilcoxon rank sum w/ Bonferroni). VISp: primary visual cortex; RSPv: ventral retrosplenial cortex; ACAd: dorsal anterior cingulate cortex; CA1: cornu ammonis hippocampus; WT: wild-type; APP: amyloid precursor protein and mutant human presenilin 1; NREM: non-rapid eye movement sleep; REM: rapid eye movement sleep.

bioRxiv preprint doi: https://doi.org/10.1101/2022.11.14.516510; this version posted November 14, 2022. The copyright holder for this preprint (which was not certified by peer review) is the author/funder, who has granted bioRxiv a license to display the preprint in perpetuity. It is made available under aCC-BY-NC-ND 4.0 International license.

FIGURE 2

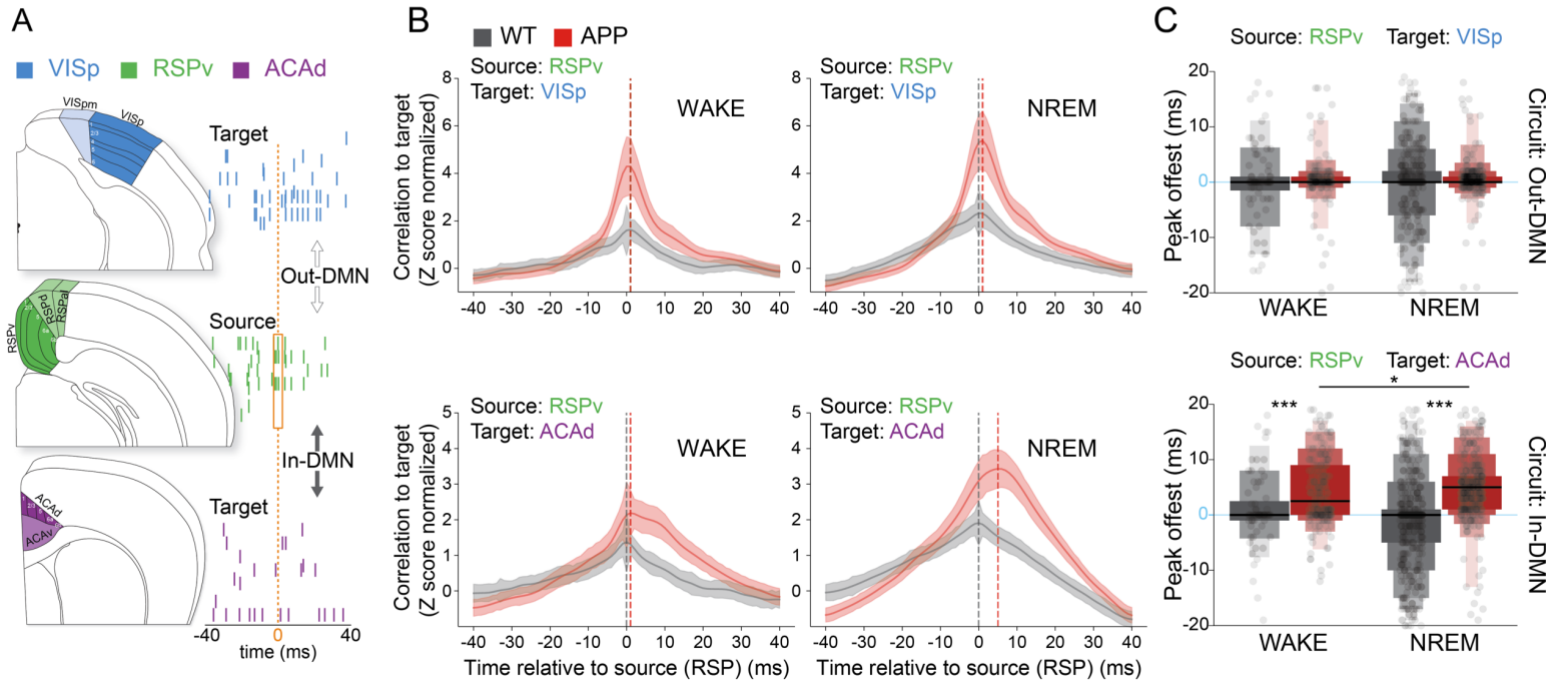

Figure 2: Inter-regional spike timing during sleep is disrupted in in-DMN circuitry. A) Cartoon illustrating source/target correlation analysis. Single neuron activity in RSPv is correlated with single neuron activity in each of two targets, i.e., the timing spike synchrony is measured between two regions. B) (top) The timing of out-DMN synchrony does not vary as a function of genotype or brain state. (bottom) In-DMN circuitry shows a delay in ACAd activity relative to RSPv that is enhanced in NREM sleep. C) Quantification of the time difference between source and target peaks. (top) There are no significant differences between genotypes in out-DMN circuit timing in either wake or NREM sleep. (bottom) Relative to WT, APP target activity is delayed significantly in wake and NREM. The delay in NREM is significantly greater than the delay in wake (* $p < 0.05$, *** $p < 0.001$ Wilcoxon rank sum w/ Bonferroni).

bioRxiv preprint doi: https://doi.org/10.1101/2022.11.14.516510; this version posted November 14, 2022. The copyright holder for this preprint (which was not certified by peer review) is the author/funder, who has granted bioRxiv a license to display the preprint in perpetuity. It is made available under aCC-BY-NC-ND 4.0 International license.

FIGURE 3

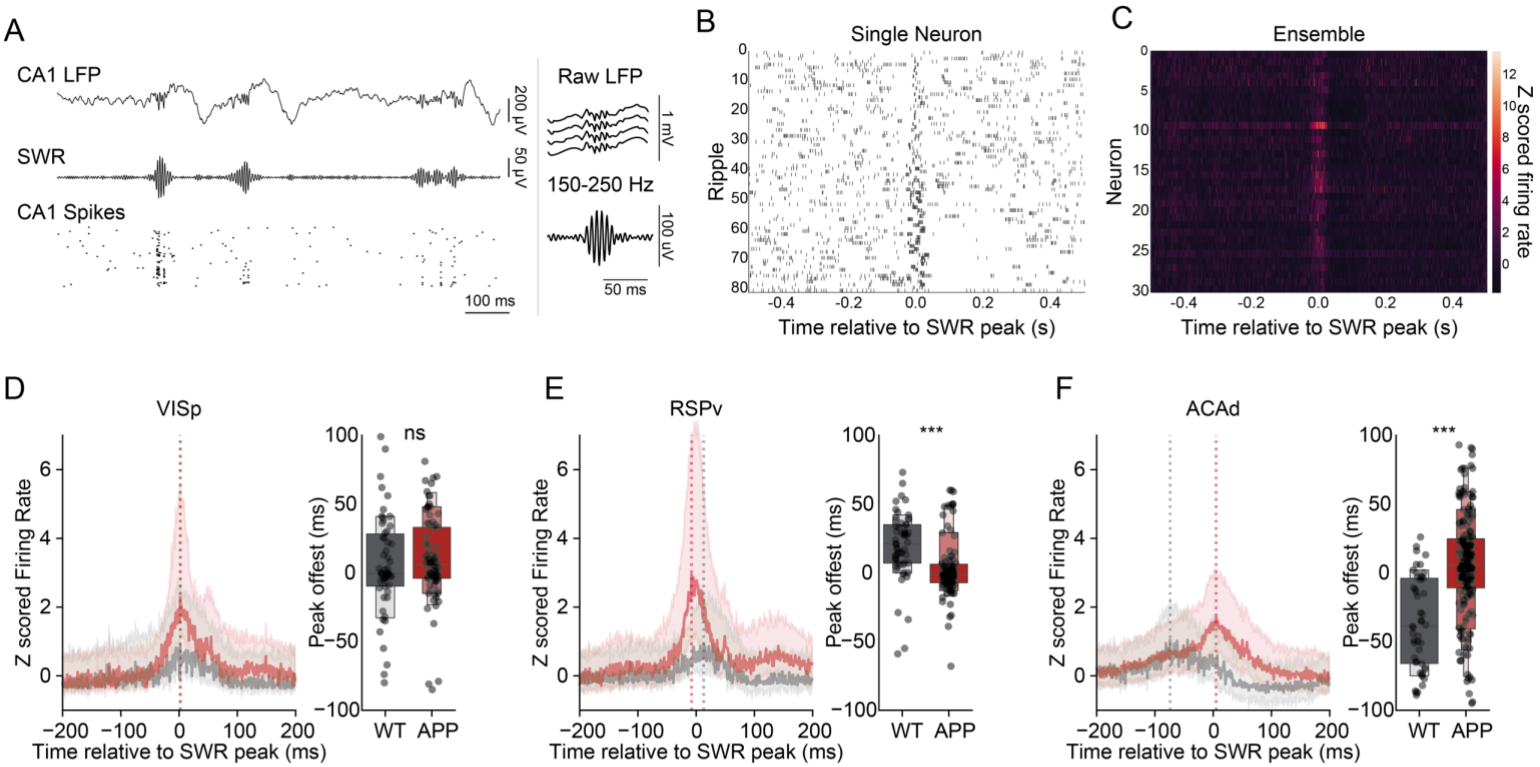

Figure 3: The timing of sharp-wave ripple-driven activity is disrupted only in the DMN. A) (left) Example sharp wave ripples (SWRs) shown in: (top) raw local field potential (LFP) recorded in CA1, (middle) 150-250 Hz bandpassed data, and (bottom) CA1 single unit activity. (right, top) A single SWR in raw data, and (right, bottom) band-passed data. B) Raster plot of the response of a CA1 single unit to 80 SWRs. C) The average response of 30 single units to SWRs. D) The timing of single unit activity during SWRs in VISp does not differ by genotype. (left) Peri-ripple histogram across units from all mice, (right) distributions of peaks by genotype. (Wilcoxon rank sum n.s. not significant, *** $p < 0.001$) E) RSPv single unit activity during SWRs is significantly accelerated compared to WT. F) ACAd single unit activity during SWRs is significantly delayed relative to WT.

bioRxiv preprint doi: https://doi.org/10.1101/2022.11.14.516510; this version posted November 14, 2022. The copyright holder for this preprint (which was not certified by peer review) is the author/funder, who has granted bioRxiv a license to display the preprint in perpetuity. It is made available under aCC-BY-NC-ND 4.0 International license.

FIGURE 4

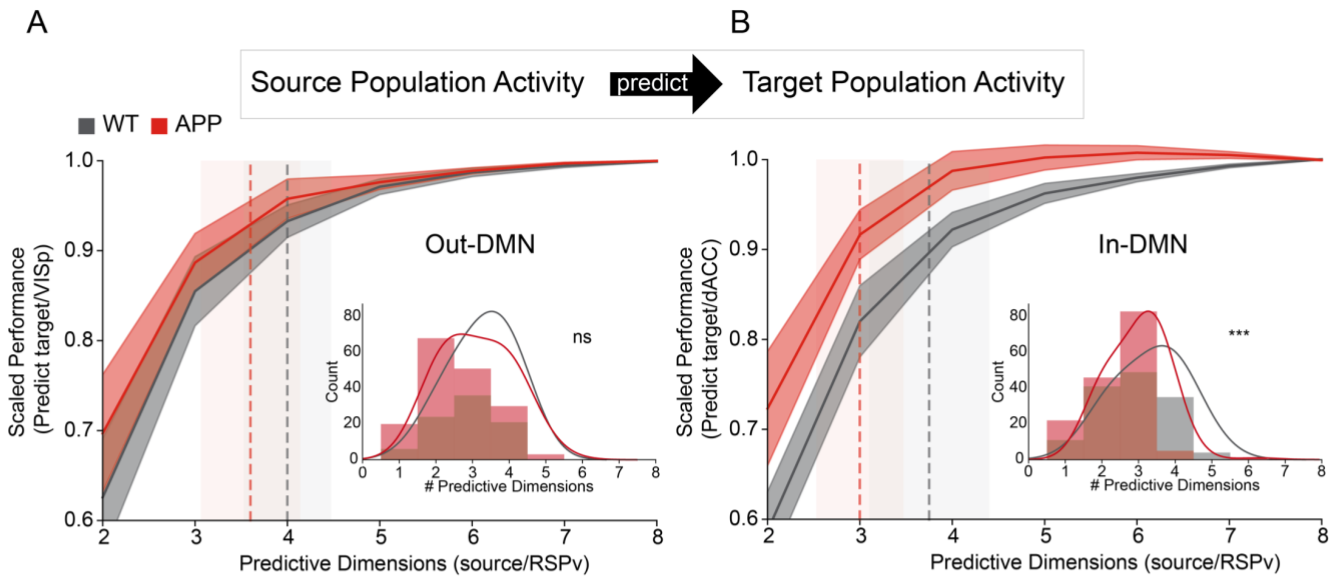

Figure 4: Single unit communication along in-DMN circuitry displays reduced dimensionality. The SWR-related activity of the entire population of single units in RSPv is used to predict population activity in two targets, VISp (out-DMN circuit) and ACAd (in-DMN circuit). The performance of the prediction is then evaluated as the dimensionality of the RSPv activity is systematically decreased. The number of dimensions at which predictive performance drops below that of the full population (plus error) is taken as the optimal dimensionality of the ensemble with regards to each target. (Left) Dimensionality of communication during SWRs in the out-DMN pathway does not vary as a function of genotype. Dashed vertical lines show median optimal dimensionality. Inset: histogram of optimal dimensions as a function of genotype (bootstrapped). Normalized kernel density estimate is overlaid. (Right) Same as left but for in-DMN pathway. Dimensionality of in-DMN pathway communication is significantly reduced in APP/PS1 animals (*** $p < 0.001$ Wilcoxon rank sum).

bioRxiv preprint doi: https://doi.org/10.1101/2022.11.14.516510; this version posted November 14, 2022. The copyright holder for this preprint (which was not certified by peer review) is the author/funder, who has granted bioRxiv a license to display the preprint in perpetuity. It is made available under aCC-BY-NC-ND 4.0 International license.

FIGURE S1

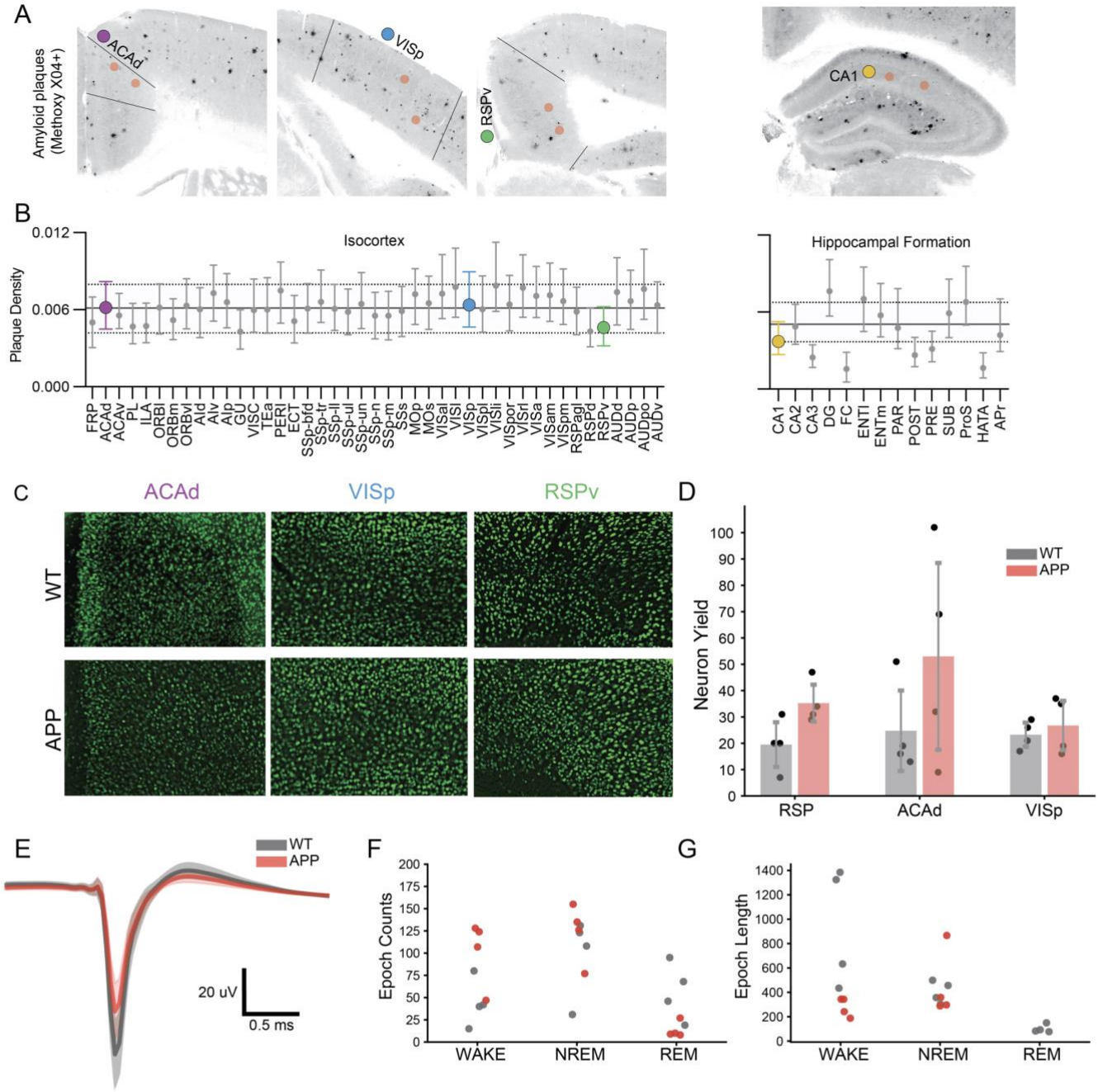

Supplemental Figure 1: Global amyloid and electrode histology. Plaque density across all cortical and hippocampal brain regions of 12–15-month-old APP/PS1 mice. Plaques were labeled with methoxy-X04 and imaged across the entire brain using serial two-photon tomography. **A** Representative images show typical plaque burden in the three cortical and hippocampal sites where electrodes were implanted in this study. Red circles indicate reconstructed electrode implantation sites from two animals. **B** Plaque densities measured with automated segmentation and registration for n=160 12–15-month-old APP/PS1 mice are plotted for all 43 isocortical and 14 hippocampal formation regions annotated in the Allen CCFv3 (Whitesell et al. 2019; Wang et al. 2020). Plots show the median and interquartile range (IQR). Solid and dashed lines show the median plaque density and IQR for the entire isocortex or hippocampal formation. **C** Representative NeuN histology from each genotype. **D** Single unit yield for each recorded region. No significant differences were found (n = animal; Wilcoxon rank sum p = 0.061 RSP, p = 0.386 ACAd, p = 0.773 VISp). **E** Average spike waveform for single units across genotypes **F** Epoch counts of each sleep state (n = animal) **G** Average epoch length of each sleep state (n = animal)

bioRxiv preprint doi: https://doi.org/10.1101/2022.11.14.516510; this version posted November 14, 2022. The copyright holder for this preprint (which was not certified by peer review) is the author/funder, who has granted bioRxiv a license to display the preprint in perpetuity. It is made available under aCC-BY-NC-ND 4.0 International license.

FIGURE S2

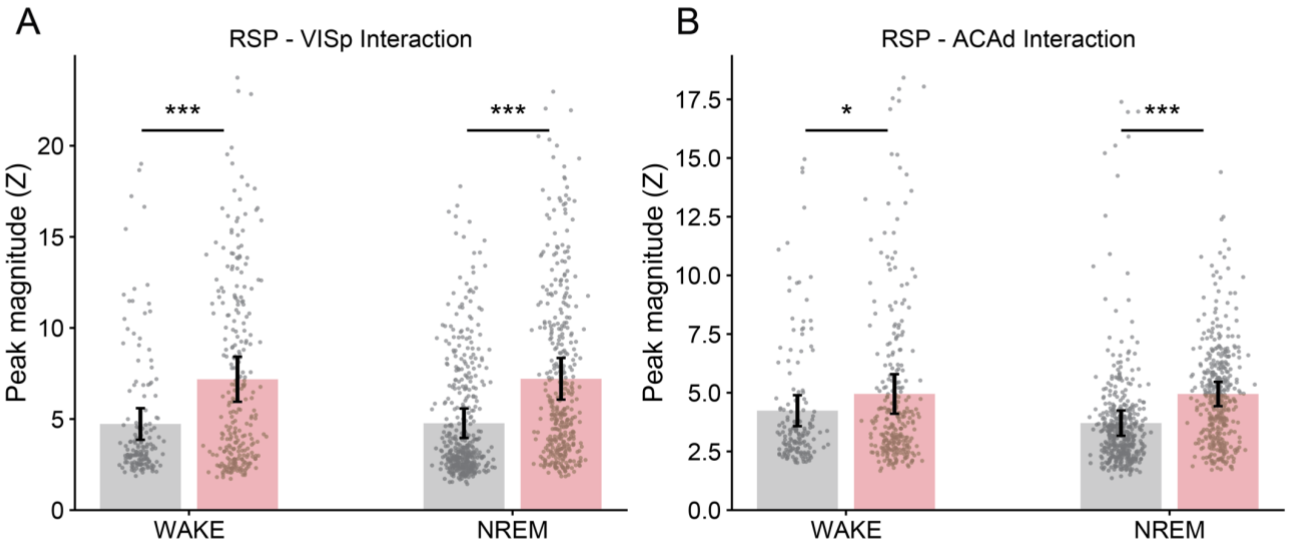

Supplemental Figure 2: Magnitude of correlation peak by circuit. **A** Peak of correlation z normalized in Wake and NREM (n = epochs) for RSP-VISp lagged correlation (Wilcoxon rank sum with Bonferroni correction p = 3e-06 Wake, p = 0.00 NREM). **B** Peak z normalized correlation in Wake and NREM (n = sleep/wake epochs) for RSP-ACAd lagged correlation (Wilcoxon rank sum with Bonferroni correction p = 0.018 Wake, p = 0.00 NREM).

bioRxiv preprint doi: https://doi.org/10.1101/2022.11.14.516510; this version posted November 14, 2022. The copyright holder for this preprint (which was not certified by peer review) is the author/funder, who has granted bioRxiv a license to display the preprint in perpetuity. It is made available under aCC-BY-NC-ND 4.0 International license.

FIGURE S3

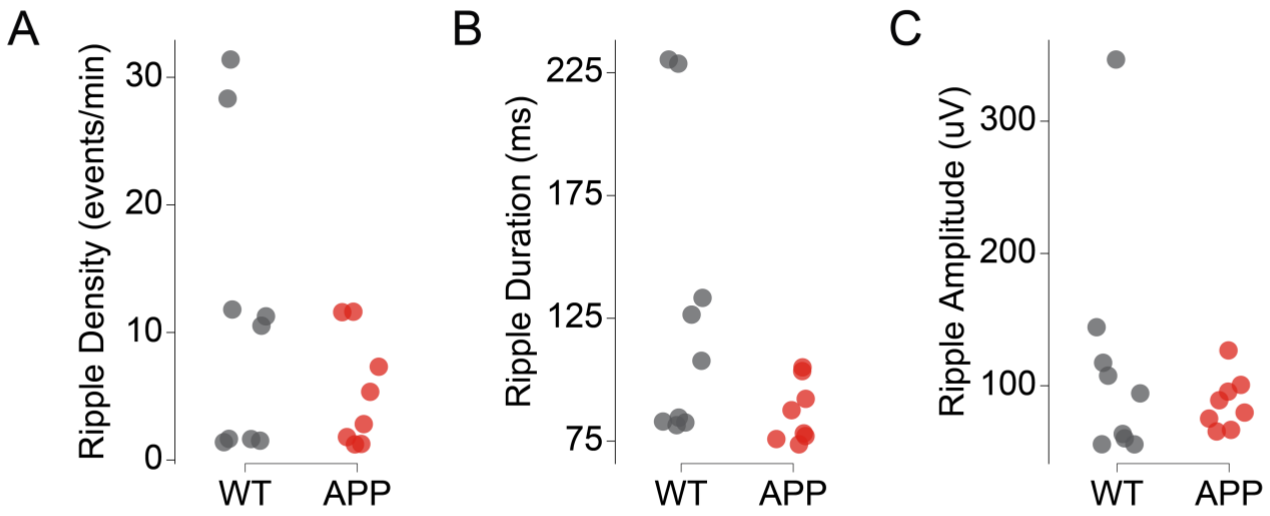

Supplemental Figure 3: Sharp wave ripple statistics across genotype. **A** Average ripple density across genotype (n = recording epoch; not significant Wilcoxon rank sum) **B** Average ripple duration across genotype (n = recording epoch; not significant Wilcoxon rank sum) **C** Average ripple amplitude across genotype (n = recording epoch; not significant Wilcoxon rank sum) **D-F** Peak magnitude of z scored firing rate around sharp wave ripple (n = single units, * $p < 0.05$, ** $p < 0.01$, n.s. not significant Wilcoxon rank sum) in **D** RSP, **E** ACAd, and **F** VISp.

bioRxiv preprint doi: https://doi.org/10.1101/2022.11.14.516510; this version posted November 14, 2022. The copyright holder for this preprint (which was not certified by peer review) is the author/funder, who has granted bioRxiv a license to display the preprint in perpetuity. It is made available under aCC-BY-NC-ND 4.0 International license.

METHODS

Animal husbandry and model

All procedures involving mice were performed in accordance with protocols approved by the Washington University in Saint Louis Institutional Animal Care and Use Committee, following guidelines described in the US National Institutes of Health Guide for the Care and Use of Laboratory Animals. We used 4 heterozygous APP+/- mice and 4 nontransgenic littermates (APP-/-) from the transgenic APP/PS1 line (B6.Cg-Tg[APPswe, PSEN1dE9]85Dbo/Mmjax, MMRRC Stock No: 034832-JAX; Jankowsky et al., 2004). All mice were between 12-16 months of age at time of experiment. Mice were housed in an enriched environment and kept on a 12:12 h light:dark cycle with ad libitum access to food and water.

Surgical procedures

All mice underwent multisite electrode array implantation surgery. Mice were anesthetized with inhaled isoflurane (1-2% in air) and administered slow release buprenorphine (ZooPharm, 0.1 mg kg^{-1}) for analgesia. The mouse's skull was secured in a robotic stereotaxic instrument (NeuroStar, Tubingen, Germany), and the skin and periosteum covering the dorsal surface of the skull was removed. Lambda and bregma midline positions were identified and used as reference coordinates for alignment with stereotaxic atlases using Neurostar StereoDrive software. Four craniotomies (diameter 1-1.5 mm) were drilled over target implantation sites using the automatic drilling function of the stereotaxic robot, and the dura mater membrane was resected. Four brain regions were implanted with custom 64-channel nichrome tetrode-based arrays cut at a 45 degree angle such that the distance between the shortest and longest tetrode was 350-500 µm. Arrays were fixed (not drivable) and separated from headstage hardware by a flex cable, thus allowing an arbitrary geometry of multiple probes. In each mouse, four 64 channel arrays were targeted so that the longest recording wire was centered on the following stereotaxic coordinates (AP/ML/DV relative to bregma and dura, in mm): CA1 (-2.52/-1.75/1.5), ACAd (0.6/-0.25/1.15), RSPv (-3.28/-0.95/1.17), and VISp (-4.03/-2.88/1.25). Electrode bundles were lowered into brain tissue at a rate of 3 mm/min using a custom built vacuum holder. Anatomical location was confirmed post hoc via histological reconstruction. Arrays were secured with dental cement (C&B-Metabond Quick! Luting Cement, Parkell Products Inc; Flow-It ALC Flowable Dental Composite, Pentron), and headstage electronics (eCube, White Matter LLC) were bundled and secured in custom 3D-printed housing. Four-module (256 channel) implants weighed approximately 2 g. Post surgery, mice were administered meloxicam (Pivetal, 5 mg kg^{-1} day^{-1} for three days) and dexamethasone (0.5 mg kg^{-1} day^{-1} for three days) and allowed to recover in the recording chamber prior to recording.

Recording procedures

Recordings were made using custom tetrode-based arrays. Sixteen tetrodes (64 channels) were soldered to a custom-designed PCB (5 mm x 5 mm x 200 µm) which stacked horizontally with a similarly sized amplifier chip (White Matter LLC, Seattle). PCB/amplifier pairs further stacked with 3 additional pairs (total 4 modules, 256 channels). Recordings were conducted in an enriched home cage environment with social access to a litter mate through a perforated acrylic divider. Freely behaving mice were attached to a custom built cable with in-line commutation. Neuronal signals were amplified, digitized, and sampled at 25 kHz alongside synchronized 15-30 fps video using the eCube Server electrophysiology system (White Matter LLC). Recordings were conducted continuously for between two weeks and three months. Data and video were continuously monitored using Open Ephys (Siegle et al., 2017) and Watch Tower (White Matter LLC). 24 h blocks of data were identified for inclusion in these studies first by the absence of hardware and/or software

bioRxiv preprint doi: https://doi.org/10.1101/2022.11.14.516510; this version posted November 14, 2022. The copyright holder for this preprint (which was not certified by peer review) is the author/funder, who has granted bioRxiv a license to display the preprint in perpetuity. It is made available under aCC-BY-NC-ND 4.0 International license.

problems, for example cable disconnects or dropped video frames, respectively, and second by the maximal yield of active channels. Beyond these criteria, selection of 24 h blocks was arbitrary.

For experiments involving spike-sorted data, raw data were bandpass filtered between 350 and 7,500 Hz and spike waveforms were extracted and clustered using a modified version of SpikeInterface (Buccino et al., 2020) and MountainSort4 (Chung et al., 2017) with curation turned off. A custom XGBoosted decision tree was used to identify those clusters constituting single units. Clusters identified as single units were manually inspected to confirm the presence of high amplitude spiking, stable spike amplitude over time, consistent waveform shapes, and little to no refractory period contamination. For all downstream analyses, we excluded neurons with firing rates < 0.5 Hz or presence ratio < 0.8 throughout the duration of a sleep/wake epoch.

Probe Localization

Following recording, mice were perfused with 4% formaldehyde (PFA), the brain was extracted and immersion fixed for 24h at 4° C in PFA. Brains were then transferred to a 30% sucrose solution in PBS and stored at 4° C until brains sank. Brains were then sectioned at 50 µm on a cryostat. Sections were rinsed in PBS prior to mounting on charged slides (SuperFrost Plus, Fisher) and stained with cresyl violet. Stained sections were aligned with the Allen Institute Mouse Brain Atlas (Allen Institute for Brain Science , 2011) and tetrode tracks were identified under a microscope (Fig S1A).

Sleep wake scoring

LFP was extracted in the 0.1-60 Hz range from 5 manually selected channels for each subject. Channels were averaged together and then spectrograms were generated in 1-hour increments. Sleep scoring was performed semi-manually in custom GUI software based on spectrogram data and movement tracking of the headstage generated with DeepLabCut (Mathis et al., 2018). A random forest trained on sleep scores from multiple human raters was used to assign sleep scores in 4 s epochs from spectrogram and movement data. These were checked manually by human raters and corrected where appropriate. For periods where sleep state could not be easily discerned by spectrogram and movement alone, temporally aligned video was consulted. For downstream analyses, we only included sleep/wake epochs of duration longer than 20 s to avoid epochs dominated by the effects of state transitions.

Single Unit FR and Correlation Analysis

For each single unit, the average number of spikes was calculated in 1s bins across each epoch. Then the mean firing rate was calculated across all epochs of a particular sleep state for each neuron individually. For each sleep epoch, spikes were binned in 1 ms windows for source and target regions. The Pearson correlation was calculated between the binned spike time series for each source-target pair of units at lags from -80 to +80 ms to generate a lagged correlogram. The mean of all lagged correlograms for every pair of source-target units was calculated for each epoch. Only epochs of greater than 60 s duration were included, after which correlograms were z-scored from the mean and standard deviation of the 20 ms flanks of the correlogram (-80:-60 ms, +60:+80 ms). Z-scored correlograms were then smoothed with 2 ms Gaussian kernel for visualization. For each epoch's lagged correlogram, the peak position was found by identifying the time lag at which the maximum of the correlogram trace occurred on the z-scored correlogram in a 40 ms window around the center (-20:+20 ms).

Ripple Detection

bioRxiv preprint doi: https://doi.org/10.1101/2022.11.14.516510; this version posted November 14, 2022. The copyright holder for this preprint (which was not certified by peer review) is the author/funder, who has granted bioRxiv a license to display the preprint in perpetuity. It is made available under aCC-BY-NC-ND 4.0 International license.

For ripple detection, data from CA1 probes was downsampled to 1500 Hz and notch filtered at harmonics of 60 Hz to eliminate 60 cycle noise (60, 120, 180, 240, 300 Hz) (Liu et al., 2022). The four channels with the lowest contamination in the ripple band were selected by determining the lowest mean bandpower in the ripple band (150-250 Hz) in 5 minute windows. Signal from the four selected channels was then bandpass filtered between 150 and 250 Hz before performing ripple detection with a publicly available Python package (github.com/Eden-Kramer-Lab/ripple_detection) implementing ripple detection from Karlsson and Frank (2009). Ripple amplitude was calculated as the difference between the maximum and minimum values of the ripple band-filtered LFP signal during each ripple. Only ripples with amplitude > 50 uV were included in downstream analyses. Ripples less than 100 ms apart were combined.

To calculate peri-event time histograms (PETHs) around sharp-wave ripples, single units were separated by putative cell type using spike waveform characteristics (RSU and FS). The PETH was then calculated by summing all spike events for each unit in a given region in a 1 s bin around each ripple time occurring during a NREM epoch. PETHs were then averaged across ripples for each unit. Average PETHs were then z scored using the flanks of the PETH (-30%:+30%) to enable comparison across animals/recording epochs. All z scored PETHs from all single units of a given cell type and region were then averaged together. To ensure that only responsive cells were included in genotype comparisons, only PETHs with activity two standard deviations above PETH flank activity were used in statistical comparison.

Communication Subspace Analysis

For each recording epoch and animal, spike data from each region was aligned around NREM ripples and binned in 100 ms bins in a 1s window around each ripple. The average peri-ripple time histogram across all ripples was subtracted from each individual peri-ripple time histogram. Each peri-ripple time histogram was then z scored to account for trial-to-trial variance, and then concatenated into one final time series for each recording epoch.

From this preprocessed data, communication subspace analysis was performed using MATLAB code adapted from Semedo et al. (2019) (github.com/joao-semedo/communication-subspace). Briefly, reduced rank regression was performed between source RSP activity and target activity from VISp and ACAd. If data was rank deficient, non-contributory units were found via QR decomposition and removed. Only datasets with more than 10 units were used for subsequent reduced rank regression. To ensure that source and target contained equal numbers of units, units were randomly sampled from the larger dataset of either source or target data across 25 bootstraps to match the size of the smaller dataset. Reduced rank regression was then performed across 10 predictive dimensions using 10-fold cross validation. Optimal dimensionality was calculated as the number of predictive dimensions needed to perform within 1 standard deviation of performance at full rank (Semedo et al., 2019). Reduced rank regression was performed using the RidgeInit and Scaling parameters available in the Semedo MATLAB code. Normalized squared error was used for the loss function (sum of squared errors divided by the total sum of squares of the target data).

Results from each bootstrap were used in comparison of optimal dimensionality across genotypes. To ensure that analysis only contained reduced rank regression results where performance improved with increasing rank, RRR performance curves were included if performance at full rank was higher than performance at lowest rank and if performance at full rank was non-negative. The predictive dimensions – performance relationship curve was min-max scaled from 0 to 1 for each curve in order to make comparison across recording epochs and animals feasible.

Statistical Analyses

bioRxiv preprint doi: https://doi.org/10.1101/2022.11.14.516510; this version posted November 14, 2022. The copyright holder for this preprint (which was not certified by peer review) is the author/funder, who has granted bioRxiv a license to display the preprint in perpetuity. It is made available under aCC-BY-NC-ND 4.0 International license.

Data are reported as mean ± SEM unless otherwise noted. Significance testing was performed with Wilcoxon rank-sum test with Bonferroni post hoc correction where appropriate. All tests were performed with a significance threshold set at $p<0.05$.

Data Availability

The datasets generated and/or analyzed in this study constitute ~100 terabytes of raw neural broadband. The data are stored in a cost efficient manner not immediately accessible to the internet. Data are available upon request.

Code Availability

All relevant code from our lab, including software needed to run recordings like ours is in Python and is publicly available at github.com/hengenlab. Code necessary for the analyses used in this paper are available at github.com/hengenlab/appps1. Other groups' code including Open Ephys, SpikeInterface, MountainSort4, DeepLabCut, RippleDetection, and Communication Subspace is publicly available as specified in Methods.

Acknowledgments

This work is supported by NIH BRAIN Initiative R01NS118442 (KBH), 1R01EB029852 (ELD, KBH), BrightFocus Foundation Standard Award 29225 (KBH), and in part by the National Institute on Aging R01AG047589 (J.A.H). We thank Erik Herzog, Charles Zorumski, and Erik Muziek for mentorship and consultation, Yifan Xu for assistance with sleep scoring pipeline, Gemechu Bekele and Anna Jasper (of the Adam Kohn Lab) for assistance with communication subspace analysis, and Ravi Chopra and Bryan Higashikubo for editing and review of the manuscript. We thank David Borchelt for sharing APP/PS1 mice.

Author Contributions

S.B. assisted in recordings, performed data preprocessing, designed experiments, performed statistical analysis, and wrote the manuscript. C.F. performed surgeries and recordings. H.F. performed histology. K.B.N. provided technical consultation and software pipelines for data preprocessing. J.W. and J.A.H. contributed to initial concept, mentorship, and consultation. E.L.D. provided mentorship and assisted in writing the manuscript. K.B.H. lead and directed the project, produced figures, and wrote the manuscript.

bioRxiv preprint doi: https://doi.org/10.1101/2022.11.14.516510; this version posted November 14, 2022. The copyright holder for this preprint (which was not certified by peer review) is the author/funder, who has granted bioRxiv a license to display the preprint in perpetuity. It is made available under aCC-BY-NC-ND 4.0 International license.

References

Agosta, F., Pievani, M., Geroldi, C., Copetti, M., Frisoni, G. B., & Filippi, M. (2012). Resting state fMRI in Alzheimer's disease: beyond the default mode network. Neurobiology of aging, 33(8), 1564-1578.

Allen Institute for Brain Science (2011) Allen Reference Atlas – Mouse Brain [brain atlas]. Available from atlas.brain-map.org.

Alves, P. N., Foulon, C., Karolis, V., Bzdok, D., Margulies, D. S., Volle, E., & Thiebaut de Schotten, M. (2019). An improved neuroanatomical model of the default-mode network reconciles previous neuroimaging and neuropathological findings. Communications biology, 2(1), 1-14.

Bokenberger K, Sjölander A, Dahl Aslan AK, Karlsson IK, Åkerstedt T, Pedersen NL. Shift work and risk of incident dementia: a study of two population-based cohorts. Eur J Epidemiol. 2018 Oct;33(10):977-987. doi: 10.1007/s10654-018-0430-8. Epub 2018 Aug 3. PMID: 30076495; PMCID: PMC6153510.

Braak, Heiko, Johannes Brettschneider, Albert C. Ludolph, Virginia M. Lee, John Q. Trojanowski, and Kelly Del Tredici. “Amyotrophic Lateral Sclerosis—a Model of Corticofugal Axonal Spread.” Nature Reviews. Neurology 9, no. 12 (December 2013): 708–14. https://doi.org/10.1038/nrneurol.2013.221.

Braak H, Braak E. Neuropathological stageing of Alzheimer-related changes. Acta Neuropathol. 1991;82(4):239-59. doi: 10.1007/BF00308809. PMID: 1759558.

Buccino AP, Hurwitz CL, Garcia S, Magland J, Siegle JH, Hurwitz R, Hennig MH. SpikeInterface, a unified framework for spike sorting. Elife. 2020 Nov 10;9:e61834. doi: 10.7554/eLife.61834. PMID: 33170122; PMCID: PMC7704107.

Busche, Marc Aurel, Gerhard Eichhoff, Helmuth Adelsberger, Dorothee Abramowski, Karl-Heinz Wiederhold, Christian Haass, Matthias Staufenbiel, Arthur Konnerth, and Olga Garaschuk. “Clusters of Hyperactive Neurons Near Amyloid Plaques in a Mouse Model of Alzheimer’s Disease.” Science 321, no. 5896 (September 19, 2008): 1686–89. https://doi.org/10.1126/science.1162844.

Busche, Marc Aurel, Xiaowei Chen, Horst A. Henning, Julia Reichwald, Matthias Staufenbiel, Bert Sakmann, and Arthur Konnerth. “Critical Role of Soluble Amyloid-β for Early Hippocampal Hyperactivity in a Mouse Model of Alzheimer’s Disease.” Proceedings of the National Academy of Sciences 109, no. 22 (May 29, 2012): 8740–45. https://doi.org/10.1073/pnas.1206171109.

Cardin, J.A., Palmer, L.A., and Contreras, D. (2007). Stimulus feature selectivity in excitatory and inhibitory neurons in primary visual cortex. J. Neurosci. 27, 10333–10344.

Chen X, Fischer S, Zhang A, Gillis J, Zador AM (2022). Modular cell type organization of cortical areas revealed by in situ sequencing. bioRxiv 2022.11.06.515380; doi: doi.org/10.1101/2022.11.06.515380

Chung, J. E., Magland, J. F., Barnett, A. H., Tolosa, V. M., Tooker, A. C., Lee, K. Y., ... & Greengard, L. F. (2017). A fully automated approach to spike sorting. Neuron, 95(6), 1381-1394.

Clark, Camilla N., and Jason D. Warren. “A Hypnic Hypothesis of Alzheimer’s Disease.” Neurodegenerative Diseases 12, no. 4 (2013): 165–76. https://doi.org/10.1159/000350060.

Cushing, Sarah D., Ivan Skelin, Shawn C. Moseley, Alina C. Stimmell, Jessica R. Dixon, Andreza S. Melilli, Leonardo Molina, Bruce L. McNaughton, and Aaron A. Wilber. “Impaired Hippocampal-Cortical Interactions during Sleep in a Mouse Model of Alzheimer’s Disease.” Current Biology 30 (2020): 2588-2601.e5. https://doi.org/10.1016/j.cub.2020.04.087.

Girardeau, G., Benchenane, K., Wiener, S. I., Buzsáki, G., & Zugaro, M. B. (2009). Selective suppression of hippocampal ripples impairs spatial memory. Nature neuroscience, 12(10), 1222-1223.

Greicius, Michael D., Kaustubh Supekar, Vinod Menon, and Robert F. Dougherty. “Resting-State Functional Connectivity Reflects Structural Connectivity in the Default Mode Network.” Cerebral Cortex (New York, NY) 19, no. 1 (January 2009): 72–78. https://doi.org/10.1093/cercor/bhn059.

Hagmann, P., Cammoun, L., Gigandet, X., Meuli, R., Honey, C.J., Wedeen, V.J., and Sporns, O. (2008). Mapping the structural core of human cerebral cortex. PLoS Biol. 6, e159.

bioRxiv preprint doi: https://doi.org/10.1101/2022.11.14.516510; this version posted November 14, 2022. The copyright holder for this preprint (which was not certified by peer review) is the author/funder, who has granted bioRxiv a license to display the preprint in perpetuity. It is made available under aCC-BY-NC-ND 4.0 International license.

Hengen, Keith B., Alejandro Torrado Pacheco, James N. McGregor, Stephen D. Van Hooser, and Gina G. Turrigiano. "Neuronal Firing Rate Homeostasis Is Inhibited by Sleep and Promoted by Wake." Cell 165, no. 1 (March 2016): 180–91. https://doi.org/10.1016/j.cell.2016.01.046.

Hengen, Keith B., Mary E. Lambo, Stephen D. Van Hooser, Donald B. Katz, and Gina G. Turrigiano. "Firing Rate Homeostasis in Visual Cortex of Freely Behaving Rodents." Neuron 80, no. 2 (October 16, 2013): 335–42. https://doi.org/10.1016/j.neuron.2013.08.038.

Horn, A., Ostwald, D., Reisert, M., and Blankenburg, F. (2014). The structural functional connectome and the default mode network of the human brain. Neuroimage 102, 142–151.

Hsia, A. Y., E. Masliah, L. McConlogue, G. Q. Yu, G. Tatsuno, K. Hu, D. Kholodenko, R. C. Malenka, R. A. Nicoll, and L. Mucke. "Plaque-Independent Disruption of Neural Circuits in Alzheimer's Disease Mouse Models." Proceedings of the National Academy of Sciences of the United States of America 96 6 (1999): 3228–33. https://doi.org/10.1073/PNAS.96.6.3228.

Jones, D. T., Knopman, D. S., Gunter, J. L., Graff-Radford, J., Vemuri, P., Boeve, B. F., ... & Jack Jr, C. R. (2016). Cascading network failure across the Alzheimer's disease spectrum. Brain, 139(2), 547-562.

Ju, Y. E. S., McLeland, J. S., Toedebusch, C. D., Xiong, C., Fagan, A. M., Duntley, S. P., ... & Holtzman, D. M. (2013). Sleep quality and preclinical Alzheimer disease. JAMA neurology, 70(5), 587-593.

Jucker, Mathias, and Lary C. Walker. "Self-Propagation of Pathogenic Protein Aggregates in Neurodegenerative Diseases." Nature 501, no. 7465 (September 5, 2013): 45–51. https://doi.org/10.1038/nature12481.

Jura, Bartosz, Nathalie Macrez, Pierre Meyrand, and Tiaza Bem. "Deficit in Hippocampal Ripples Does Not Preclude Spatial Memory Formation in APP/PS1 Mice." Scientific Reports 9, no. 1 (December 27, 2019): 20129. https://doi.org/10.1038/s41598-019-56582-w.

Kadowaki, H., Nishitoh, H., Urano, F., Sadamitsu, C., Matsuzawa, A., Takeda, K., ... & Ichijo, H. (2005). Amyloid β induces neuronal cell death through ROS-mediated ASK1 activation. Cell Death & Differentiation, 12(1), 19-24.

Kaefer, Karola, Federico Stella, Bruce L. McNaughton, and Francesco P. Battaglia. "Replay, the Default Mode Network and the Cascaded Memory Systems Model." Nature Reviews Neuroscience 23, no. 10 (October 2022): 628–40. https://doi.org/10.1038/s41583-022-00620-6.

Karlsson MP, Frank LM. Awake replay of remote experiences in the hippocampus. Nat Neurosci. 2009 Jul;12(7):913-8. doi: 10.1038/nn.2344. Epub 2009 Jun 14. PMID: 19525943; PMCID: PMC2750914.

Klee, Jan L., Amanda J. Kiliaan, Arto Lipponen, and Francesco P. Battaglia. "Reduced Firing Rates of Pyramidal Cells in the Frontal Cortex of APP/PS1 Can Be Restored by Acute Treatment with Levetiracetam." Neurobiology of Aging 96 (December 1, 2020): 79–86. https://doi.org/10.1016/j.neurobiolaging.2020.08.013

Lim, Miranda M., Jason R. Gerstner, and David M. Holtzman. "The Sleep–Wake Cycle and Alzheimer's Disease: What Do We Know?" Neurodegenerative Disease Management 4, no. 5 (2014): 351–62. https://doi.org/10.2217/nmt.14.33.

Liu, Anli A., Simon Henin, Saman Abbaspoor, Anatol Bragin, Elizabeth A. Buffalo, Jordan S. Farrell, David J. Foster, et al. "A Consensus Statement on Detection of Hippocampal Sharp Wave Ripples and Differentiation from Other Fast Oscillations." *Nature Communications* 13, no. 1 (October 12, 2022): 6000. https://doi.org/10.1038/s41467-022-33536-x.

Mathis, A., Mamidanna, P., Cury, K. M., Abe, T., Murthy, V. N., Mathis, M. W., & Bethge, M. (2018). DeepLabCut: markerless pose estimation of user-defined body parts with deep learning. Nature neuroscience, 21(9), 1281-1289.

McClelland, James L, and Randall C O'Reilly. "Why There Are Complementary Learning Systems in the Hippocampus and Neocortex: Insights From the Successes and Failures of Connectionist Models of Learning and Memory," 1995, 39.

bioRxiv preprint doi: https://doi.org/10.1101/2022.11.14.516510; this version posted November 14, 2022. The copyright holder for this preprint (which was not certified by peer review) is the author/funder, who has granted bioRxiv a license to display the preprint in perpetuity. It is made available under aCC-BY-NC-ND 4.0 International license.

Minkeviciene, R., S. Rheims, M. B. Dobszay, M. Zilberter, J. Hartikainen, L. Fulop, B. Penke, et al. "Amyloid -Induced Neuronal Hyperexcitability Triggers Progressive Epilepsy." Journal of Neuroscience 29, no. 11 (March 18, 2009): 3453–62. https://doi.org/10.1523/JNEUROSCI.5215-08.2009.

Niell, Cristopher M., and Michael P. Stryker. "Highly Selective Receptive Fields in Mouse Visual Cortex." Journal of Neuroscience 28, no. 30 (July 23, 2008): 7520–36. doi.org/10.1523/JNEUROSCI.0623-08.2008.

Opalka, Ashley N., Wen-qiang Huang, Jun Liu, Hualou Liang, and Dong V. Wang. "Hippocampal Ripple Coordinates Retrosplenial Inhibitory Neurons during Slow-Wave Sleep." Cell Reports 30, no. 2 (January 14, 2020): 432-441.e3. https://doi.org/10.1016/j.celrep.2019.12.038.

Palop, Jorge J., and Lennart Mucke. "Network Abnormalities and Interneuron Dysfunction in Alzheimer Disease." Nature Reviews Neuroscience 17, no. 12 (December 2016): 777–92. doi.org/10.1038/nrn.2016.141.

Raichle, M. E., A. M. MacLeod, A. Z. Snyder, W. J. Powers, D. A. Gusnard, and G. L. Shulman. "A Default Mode of Brain Function." Proceedings of the National Academy of Sciences 98, no. 2 (January 16, 2001): 676–82. https://doi.org/10.1073/pnas.98.2.676.

Rasch, Björn, and Jan Born. "About Sleep's Role in Memory." Physiological Reviews 93, no. 2 (April 2013): 681–766. https://doi.org/10.1152/physrev.00032.2012.

Roh, J. H., Huang, Y., Bero, A. W., Kasten, T., Stewart, F. R., Bateman, R. J., & Holtzman, D. M. (2012). Disruption of the sleep-wake cycle and diurnal fluctuation of β-amyloid in mice with Alzheimer's disease pathology. Science translational medicine, 4(150), 150ra122-150ra122.

Rupp, Niels J., Bettina M. Wegenast-Braun, Rebecca Radde, Michael E. Calhoun, and Mathias Jucker. "Early Onset Amyloid Lesions Lead to Severe Neuritic Abnormalities and Local, but Not Global Neuron Loss in APPPS1 Transgenic Mice." Neurobiology of Aging 32 (2011): 2324.e1-2324.e6. https://doi.org/10.1016/j.neurobiolaging.2010.08.014

Semedo, João D., Amin Zandvakili, Christian K. Machens, Byron M. Yu, and Adam Kohn. "Cortical Areas Interact through a Communication Subspace." Neuron 102, no. 1 (April 2019): 249-259.e4. https://doi.org/10.1016/j.neuron.2019.01.026.

Shah, D., Latif-Hernandez, A., De Strooper, B., Saito, T., Saido, T., Verhoye, M., ... & Van der Linden, A. (2018). Spatial reversal learning defect coincides with hypersynchronous telencephalic BOLD functional connectivity in APPNL-F/NL-F knock-in mice. Scientific reports, 8(1), 1-11.

Sheline, Y. I., Raichle, M. E., Snyder, A. Z., Morris, J. C., Head, D., Wang, S., & Mintun, M. A. (2010). Amyloid plaques disrupt resting state default mode network connectivity in cognitively normal elderly. Biological psychiatry, 67(6), 584-587.

Siegle JH, López AC, Patel YA, Abramov K, Ohayon S, Voigts J. Open Ephys: an open-source, plugin-based platform for multichannel electrophysiology. J Neural Eng. 2017 Aug;14(4):045003. doi: 10.1088/1741-2552/aa5eea. PMID: 28169219.

Trinchese, F., Liu, S., Battaglia, F., Walter, S., Mathews, P. M., & Arancio, O. (2004). Progressive age-related development of Alzheimer-like pathology in APP/PS1 mice. Annals of Neurology: Official Journal of the American Neurological Association and the Child Neurology Society, 55(6), 801-814.

Walker, Lary C., and Mathias Jucker. "Neurodegenerative Diseases: Expanding the Prion Concept." Annual Review of Neuroscience 38 (July 8, 2015): 87–103. doi.org/10.1146/annurev-neuro-071714-033828.

Warren, Jason D., Jonathan D. Rohrer, Jonathan M. Schott, Nick C. Fox, John Hardy, and Martin N. Rossor. "Molecular Nexopathies: A New Paradigm of Neurodegenerative Disease." Trends in Neurosciences 36, no. 10 (October 2013): 561–69. https://doi.org/10.1016/j.tins.2013.06.007.

Whitesell, Jennifer D., Adam Liska, Ludovico Coletta, Karla E. Hirokawa, Phillip Bohn, Ali Williford, Peter A. Groblewski, et al. "Regional, Layer, and Cell-Type-Specific Connectivity of the Mouse Default Mode Network." Neuron 109, no. 3 (February 3, 2021): 545-559.e8. doi.org/10.1016/j.neuron.2020.11.011.

Whitesell, Jennifer D., Alex R. Buckley, Joseph E. Knox, Leonard Kuan, Nile Graddis, Andrew Pelos, Alice Mukora, et al. "Whole Brain Imaging Reveals Distinct Spatial Patterns of Amyloid Beta Deposition in

bioRxiv preprint doi: https://doi.org/10.1101/2022.11.14.516510; this version posted November 14, 2022. The copyright holder for this preprint (which was not certified by peer review) is the author/funder, who has granted bioRxiv a license to display the preprint in perpetuity. It is made available under aCC-BY-NC-ND 4.0 International license.

Three Mouse Models of Alzheimer's Disease." Journal of Comparative Neurology 527, no. 13 (September 2019): 2122–45. https://doi.org/10.1002/cne.24555.

Witton, Jonathan, Lydia E. Staniaszek, Ullrich Bartsch, Andrew D. Randall, Matthew W. Jones, and Jonathan T. Brown. "Disrupted Hippocampal Sharp-wave Ripple-associated Spike Dynamics in a Transgenic Mouse Model of Dementia." The Journal of Physiology 594, no. 16 (August 15, 2016): 4615–30. https://doi.org/10.1113/jphysiol.2014.282889.

Yamawaki, N., Li, X., Lambot, L., Ren, L. Y., Radulovic, J., & Shepherd, G. M. (2019). Long-range inhibitory intersection of a retrosplenial thalamocortical circuit by apical tuft-targeting CA1 neurons. Nature neuroscience, 22(4), 618-626.

Zarhin, Daniel, Refaela Atsmon, Antonella Ruggiero, Halit Baeloha, Shiri Shoob, Oded Scharf, Leore R. Heim, et al. "Disrupted Neural Correlates of Anesthesia and Sleep Reveal Early Circuit Dysfunctions in Alzheimer Models." Cell Reports 38, no. 3 (January 18, 2022): 110268.doi.org/10.1016/j.celrep.2021.110268.

Zhurakovskaya, E., I. Ishchenko, I. Gureviciene, R. Aliev, O. Gröhn, and H. Tanila. "Impaired Hippocampal-Cortical Coupling but Preserved Local Synchrony during Sleep in APP/PS1 Mice Modeling Alzheimer's Disease." Scientific Reports 9 (2019). doi.org/10.1038/s41598-019-41851-5.